Phase change effect on the structural and electrochemical behaviour of pure and doped vanadium pentoxide as positive electrodes for lithium ion batteries

Ceilidh F. Armer[1,2], Mechthild Lübke[2,3], M. V. Reddy[4,5], Jawwad A. Darr[3], Xu Li[2]*,

Adrian Lowe[1]*

[1] College of Engineering and Computer Science, Australian National University, Canberra, ACT 0200, Australia
[2] Institute of Materials Research and Engineering, Agency for Science, Technology and Research (A*STAR), 2 Fusionopolis Way, Innovis #08-03, Singapore 138634, Singapore
[3] Department of Chemistry, University College London, 20 Gordon Street, London, WC1H 0AJ, UK
[4] Department of Physics, National University of Singapore, Singapore 117542, Singapore
[5] Department of Materials Science and Engineering, National University of Singapore, Singapore 117576, Singapore

*Corresponding author: Dr Adrian Lowe
College of Engineering and Computer Science, Australian National University
Canberra, ACT 0200
Office telephone: +61 2 6125 4881
Email: adrian.lowe@anu.edu.au

Abstract

Electrospun ceramic oxide fibers find myriad uses as energy materials such as in battery electrodes and vanadium oxides are one such family of materials. In this study, the structural and energy storage properties of electrospun vanadium pentoxide are compared to approximately 10 at% barium and titanium-doped equivalents. The vanadium pentoxide was doped in order to improve its electrochemical performance. The materials are characterised using powder X-ray diffraction, scanning electron microscopy, energy dispersive X-ray spectroscopy, X-ray photoelectron spectroscopy, Brunauer-Emmett-Teller measurements, transmission electron microscopy and potentiostatic and galvanostatic analysis. X-ray diffraction analysis showed that each dopant has a critical effect on lattice distortions whilst showing no influence over the overall crystal structure, which is unusual for such large dopant amounts. The doped materials show better cyclability and higher efficiencies than the pure equivalent. Ex-situ X-ray diffraction measurements show detrimental phase changes within undoped V_2O_5 whereas the titanium-doped V_2O_5 predominantly remains as α-V_2O_5 after the first cycle.

Highlights

- α-V_2O_5 microfibers consist of nanoparticles fabricated through electrospinning.

- Reasonably large dopant amount into the V_2O_5 structure is possible.

- 10 at% Ti^{4+} in V_2O_5 significantly improves its electrochemical performance.

- Phase changes during cycling show substantial differences with the pure and doped V_2O_5.

Keywords: electrospinning, V_2O_5, doping, lithium ion battery, positive electrode

1.0 Introduction

Lithium ion batteries (LIBs) have made up a significant portion of the battery market for over a decade due to their long shelf life and high energy density [1]. Recent LIB research has focussed on the prevention of thermal runaway [2], lattice distortions induced by lithium (Li) ion conduction [3] during cycling, and low-temperature performance investigations [4]. Additionally, an inorganic-organic hybrid solid electrolyte achieved commercial levels of ionic conductivity and prevented electrolyte decomposition [5]. These studies increase the practical usage of LIBs by improving safety and increasing operational temperatures. Currently, most positive electrode materials can only store one Li-ion per charge, which drastically limits stored energy and leaves them susceptible to kinetic problems that arise from slow ion diffusion and poor electrical conductivity [6].

Many materials showed improved performance after nanosizing compared to the bulk due to improved Li-ion kinetics such as reduced path lengths for transport; e.g. $LiVPO_4F$ [7], $LiMn_{1.5}Ni_{0.5}O_4$ [8], $LiFePO_4$ [9], and $Li_3V_2(PO_4)_3$ [10]. Though the use of nanostructured materials often results in increased side reactions during cycling due to high surface areas during cycling [11], thus defined structures are used to enable all advantages of nanostructures [12,13]. Nanostructured fibers are of particular interest as they offer large electrolyte-electrode contact area, facile strain relaxation during cycling, short Li-ion diffusion distances, and effective electronic transport pathways for higher capacity and improved rate performance [14].

Vanadium pentoxides (V_2O_5) are potential positive electrode materials for LIBs because of their tuneable oxidation states and layered structure which reversibly intercalates Li-ion charge carriers between its layers [15]. It has an orthorhombic unit cell and is made up of bilayers consisting of stacks of distorted VO_5 square pyramids that share edges to form zigzag double chains as seen in Figure 1(a). These layers are bonded in the [001] direction (z-direction) by weak van der Waals bonds between the vanadium and oxygen of neighbouring pyramids in adjacent layers [16,17].
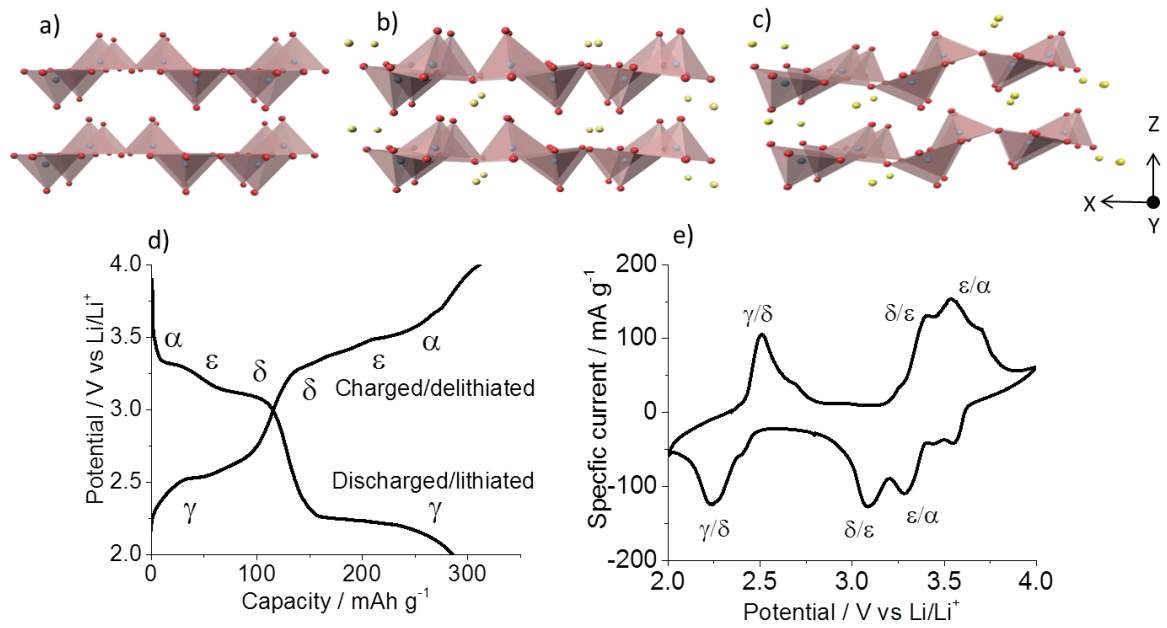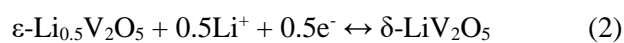
Figure 1: Structural representations of (a) α-V$_2$O$_5$ the pristine phase, (b) δ-LiV$_2$O$_5$, (c) γ-Li$_2$V$_2$O$_5$ showing different degrees of structural variations caused through Li-ion intercalation, (d) galvanostatic profile of V$_2$O$_5$ in the range of 2.0-4.0 V vs Li/Li$^+$ and e) cyclic voltammetry trace of V$_2$O$_5$ in the range of 2.0-4.0 V vs Li/Li$^+$ with relevant phases labelled.

Electrochemically, V$_2$O$_5$ is typically examined in the range of 2.0-4.0 V vs Li/Li$^+$ potential window and displays two pairs of intercalation reactions referring to two Li-ions per cycle. The first Li-ion intercalation/extraction occurs in the range of 3.0-4.0 V vs Li/Li$^+$. In some cases, depending on material morphology, there can be strong peak splitting which suggests multiple Li-ion sites of varying energy differences for multi-stepped intercalation/extraction processes which is typical of nanoscale V$_2$O$_5$ [18] This Li-ion intercalation event occurs with oxidation reaction(s) in the range of 3.3-3.5 V vs Li/Li$^+$ and with reduction reaction(s) in the range of 3.1-3.3 V vs Li/Li$^+$ which can be described with Equations (1) and Equation (2) [18,19] and is visually represented in Figure 1(b).

$$\alpha\text{-V}_2\text{O}_5 + 0.5\text{Li}^+ + 0.5\text{e}^- \leftrightarrow \varepsilon\text{-Li}_{0.5}\text{V}_2\text{O}_5 \qquad (1)$$

$$\varepsilon\text{-Li}_{0.5}\text{V}_2\text{O}_5 + 0.5\text{Li}^+ + 0.5\text{e}^- \leftrightarrow \delta\text{-LiV}_2\text{O}_5 \qquad (2)$$

The ε-phase is similar to the non-intercalated α-V_2O_5 phase with some distortion of the V_2O_5 layers caused by gliding of the VO_5 square pyramids. The δ-LiV_2O_5 phase is also made up of V_2O_5 layers but they are substantially more distorted as the VO_5 square pyramids have shifted by half a unit cell parameter along the *b*-axis causing the *c*-parameter to increase [20]. Distortion in the δ-phase requires little energy so no V-O bonds are broken. Cheah *et. al.* conducted a detailed study into the Li-ion intercalation of V_2O_5 and observed that the structural transformation of the α-ε and ε-δ phases are reversible during cycling in the range of 2.0-4.0 V vs Li/Li^+ [21]. The second Li-ion intercalation/extraction event occurs in the range of 2.2-2.5 V vs Li/Li^+ according to Equation (3).

$$\delta\text{-}LiV_2O_5 + 1Li^+ + 1e^- \leftrightarrow \gamma\text{-}Li_2V_2O_5 \qquad (3)$$
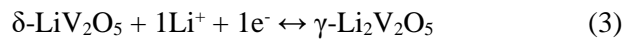
Generally, the δ-γ phase transformation is irreversible as V-O bonds must be broken during the conversion from δ-LiV_2O_5 to form the new phase and accommodate excessive Li-ion intercalation resulting in extensive bending and flexing of the vanadium oxide layers as seen in Figure 1(c). The presence of Li-ions combined with vanadium (V) ion reduction leads to a modification of the positive charge distribution within the oxygen anion array [22]. However, x Li-ions within the stoichiometric range 0<x<2 can be reversibly cycled in the metastable γ-$Li_xV_2O_5$ phase. Once this phase is formed, γ-$Li_xV_2O_5$ is retained upon further cycling [23]. These intercalation events described above can be seen with galvanostatic and potentiodynamic methods, Figure 1(d,e). Several studies have compared the electrochemical performance of commercial and nanoscale V_2O_5 and observed comparable phase transitions and shape as those described above for both types of V_2O_5. In all cases, it was shown that the nanosized V_2O_5 possessed lower polarisation and higher peak currents reflecting higher obtained capacities [18,24,25]. Despite the advantage of high theoretical capacity (294 mAh g^{-1}, equivalent to 2 M Li ions per 1 M V_2O_5), V_2O_5 is susceptible to structural variations and slow electrochemical kinetics associated with the intercalation/extraction of Li-ions resulting in poor cycle stability [15]. In addition, V_2O_5 is limited by low electrical conductivity (10^{-2} to 10^{-3} Scm^{-1}) and low Li ion diffusion coefficients (10^{-12} to 10^{-15} cm^2s^{-1}) [26].

Redox-inactive dopants (in which there is no additional redox charge transfer reactions upon lithiation/delithiation) are often used for positive electrode materials in LIBs. Lithium iron phosphate (LFP) is a very stable high power electrode material and many redox-inactive dopants have been shown to improve the cycling performance, e.g. Nb^{5+} [27], Ti^{4+} [28], and Al^{3+} [29]. The occupying site of the dopant depends on the cation and has been often shown to improve the electronic and/or ionic conductivity [29]. For lithiated transition metal oxides, one main issue is still the stability upon cycling, which can be improved by using redox-inactive cations such as Mn^{4+} or Al^{3+}. NCA ($LiNi_{0.8}Co_{0.15}Al_{0.05}O_2$) is one such example where a small amount of the redox inactive dopant Al^{3+} has been shown to improve electrochemical performance and reduce cell impedance resulting in a stabilization of both the material structure and surface reactivity [30]. The use of the Al^{3+} dopant combined with the reduction of cationic disorder caused by the partial substitution of Ni with Co [31], as Co^{3+} is not as readily reduced as Ni^{3+} [32], results in NCA having a high discharge capacity of approximately 200 mAh g^{-1}, long storage life and reduced cost compared to pure Co-based positive electrodes [33].

In terms of V_2O_5, redox-inactive dopants include, but are not limited to Cr^{3+} [17,34], Ag^+ [35,36], Cu^{2+} [37], Al^{3+} [36,38,39], Nb^{5+} [40], Na^+ [41], and Fe^{3+} [42] when studied within or near to the 2.0-4.0 V vs Li/Li^+ range. The use of Ti^{4+} as a dopant for vanadium oxides has shown improve electronic conductivity when used as electrode material for supercapacitors [43]. Ti^{4+} is a useful potential dopant as it has a valence state of 4+ and 3+ and its diameter is comparable to V^{5+} with a coordination number (CN) of six [44]. Like many of the previously mentioned dopants, alkaline earth metals, such as Ba^{2+} and Ca^{2+} are redox-inactive, meaning they do not show additional redox charge transfer during lithiation/delithiation between 2.0 to 4.0 V vs Li/Li^+. However they are often used because they have been shown to improve the cycling performance in materials such as tin oxide [45,46]. Zhan *et. al.*, showed that Cr^{3+} doped vanadium oxide, $Cr_{0.1}V_2O_{5.15}$, prepared via a sol gel method, partially prevented irreversible phase transitions of the V_2O_5 structure using a cyclic voltammetry analysis [17]. This was made apparent with irreversible redox peaks present in the V_2O_5 voltammogram plot while reversible redox peaks were seen in the $Cr_{0.1}V_2O_{5.15}$ voltammogram. Also observed was an

improvement in cycling performance compared to that of pure V_2O_5. Li-ion diffusion has been shown to increase via the use of dopants [44]. Liang *et al* showed that Na^+ doped V_2O_5 formed ß-$Na_{0.33}V_2O_5$ and resulted in improved Li-ion diffusion caused by a mesoporous flake-like structure produced via the introduction of the Na^+ dopant [41].

Electrospinning is an effective and inexpensive bottom-up nano-fabrication technique for synthesizing one dimensional fibres from sol gel solutions [47] and is beneficial to LIB technology as it is able to vary the nanoparticle morphologies [48]. During the electrospinning operation a strong electric field is applied to the tip of a capillary containing the sol gel solution which is drawn into a droplet. A continuous fine jet of solution is ejected from the capillary and moves through the electric field to deposit on the collector. The elongation of the charged droplet expelled from the tip of the needle is caused by electrostatic repulsions experienced in the bends of the lengthening droplet into a fiber which creates the nanometre-scale diameters [49]. The surface morphology and diameter of the fibres can be controlled by varying parameters such as applied potential, feed rate of the sol gel solution and sol gel components [50]. Doping is easily achieved in electrospinning as the dopant precursor can be added into the electrospinning solution resulting in a homogenously distributed dopant [35,39,51].

In the current study, Ti^{4+} and Ba^{2+} were homogeneously mixed with a vanadium oxide-based sol gel and electrospun to produce continuous microscale nanostructured fibers. The structural variations created due to the introduction of dopants were investigated along with the electrochemical properties. We observed that 10 at% Ti^{4+} doping made significant improvements on electrochemical performance and that phase changes occurring during cycling are noticeably different between pure V_2O_5 and titanium-doped V_2O_5

2.0 Experimental section

2.1 Materials

All chemicals were received and used without further purification. Sol gel components consisted of vanadium oxytripropoxide (98%, Sigma-Aldrich), ethanol (96%, Chem-Supply) and polyvinyl acetate (PVAc) (Mw 140,000; Sigma-Aldrich). Ba^{2+} was introduced *via* the addition of barium oxide (90%, AJAX Chemicals) and Ti^{4+} via titanium (IV) isopropoxide (97%, Sigma-Aldrich).

2.2 Synthesis of electrospun vanadium oxide fibers

The sol gel consisted of 1 g of vanadium oxytripropoxide, 1 g of ethanol and 0.3 g of PVAc which was prepared by stirring for ca. 3 h until the PVAc was completely dissolved forming an orange transparent viscous solution. The PVAc provided a template for the formation of the microfibers. In the sol gel method, unwanted hydrolysis of the vanadium oxytripropoxide was suppressed by limiting exposure to air and eliminating the addition of water. Consequently, prolonged stirring was not necessary.

For a 10 at% dopant amount, 0.116 g of titanium isopropoxide or 0.126 g of barium oxide were added to the vanadium oxide sol gel and stirred to obtain a homogeneous mixture. The Ti^{4+} sol gel was transparent and dark orange in appearance while the Ba^{2+} sol was a cloudy and yellow suspension. The sol gel solution was transferred into a 5 cc syringe and loaded into a syringe pump (KD Scientific 78-9100 KDS-100-CE) with the needle tip connected to a high-voltage power supply. When a potential of 22 kV was applied, the sol gel solution was injected at a feed rate of 2 mL h^{-1} from the needle and deposited on an aluminium foil collector. The as-spun fibres were collected and calcined in air in a single pyrolysis step at 500 °C for 2 h at a heating rate of 3 °C min^{-1} (furnace: SEM, SA Pty Ltd Cat No 1022).

2.3 Characterisation

Powder X-ray Diffraction (PXRD) of the microfibers was performed using a STOE diffractometer using Mo-Kα radiation (λ = 0.71 Å) over the 2θ range of 5 to 40° with a step size of 0.5° and step time of 30 s. Reference XRD data for V_2O_5 were obtained from the Inorganic Crystal Structures Database (ICSD) with collection code 60767. The space group was P*mmn* with unit cell parameters of a = 11.512 Å, b = 3.564 Å, c = 4.368 Å. Unit cell parameters of the nanostructured fibres were

determined via le Bail refinement using the Jana2006 crystallography program with the space group and unit cell parameters mentioned above as baselines. Optimisation of the unit was performed in order to reduce the goodness of fit (GOF), R_P and R_{WP} parameters. Relevant d-spacings were calculated using Bragg's Law.

Measurements of surface composition and the oxidation state of the elements were carried out using a Thermo Scientific K-Alpha X-ray photoelectron spectrometer (XPS) with a monochromatic Al-Kα source. Results were then fitted using Avantage software with the binding energies suited to carbon (285.0 eV) for V_2O_5 and to vanadium (517.4 eV) for the doped samples. Surface area measurements were determined using Brunauer-Emmett-Teller (BET) measurements with N_2 in a micrometrics Tri Star II 3012 analyser. Before measurements were the taken the powders were degassed at 120 °C (12 h) under vacuum.

Scanning electron microscope (SEM) images of the microfibers were taken with a Zeiss UltraPlus FESEM to study the extent of the morphology, fibrosity, and grain structure. Reported dimensions of the fibers in this study were determined using ImageJ via pixel counting using the scale bar for distance determination. Energy dispersive X-ray spectroscopy (EDS) point analysis was conducted on a JOEL FESEM JSM6700F to determine dopant amount.

The size and morphology of the crystallites were determined by transmission electron microscopy (TEM) using a JEOL JEM 2100 – LaB_6 filament. Images were taken with a Gatan Orius digital camera. Samples were prepared by dispersing in methanol followed by brief ultrasonication and pipetting several droplets on a 300 mesh copper film grid (Agar Scientific).

2.4 Electrochemical Testing

The prepared vanadium oxide fibers were processed into positive electrodes and incorporated into coin cells for electrochemical testing. The working electrode consisted of 80 wt% active material, 10 wt% conductive agent (carbon black, Super P 004, MMM Carbon) and 10 wt% polyvinylidene fluoride (PVDF, Kynar 761). PVDF was dissolved in N-methyl pyrrolidinone (NMP, Sigma Aldrich) overnight followed by addition of the active material and conductive agent. After ball-milling for

30 min at 500 rpm, the mixture was cast onto aluminium foil and dried for approximately 1 h at 70 °C. Working electrode discs were punched with 14 mm diameters, pressed with 1 ton of force for 30 s and once again dried overnight at 70 °C. The active material mass loadings were 0.9 ± 0.1 mg cm^{-1}.

Prepared electrodes were assembled into CR2032-type coin cells in an argon-filled glove box (MBraun) with oxygen and water levels below 3 ppm. Lithium foil (Hohsen Corp) made up the counter electrode with separators (glass microfiber filters, Whatman®,GF/B) saturated in 1 M LiPF$_6$ dissolved in a 1:1 v/v ratio of ethylene carbonate/dimethyl carbonate (EC/DMC) (1:1 v/v, Merck Selectipur LP40) as the electrolyte.

The electrochemical performance was investigated by cyclic voltammetry (CV) in the potential range of 2.0-4.0 V vs Li/Li$^+$ with a scan rate of 0.1 mV s^{-1} using a potentiostat (PGSTAT302, AUTOLAB, Metrohm). C-rate tests and long term cycling performance of the cells were analysed using a MACCOR battery tester (Model 4200) for 10 cycles at 50, 100, 300, 600, and back to 50 mA g^{-1} within a potential range of 2.0-4.0 V vs Li/Li$^+$. When Li-free materials are used as positive electrodes, such as those in this study, they are discharged first in order to lithiate the V$_2$O$_5$ [52].

3.0 Results and discussion

3.1 Morphology and structure

The electrospinning process used in this study produced fibrous materials with varying colours between the pure and doped materials. Pure V$_2$O$_5$ is bright yellow, Ba^{2+} doped material appeared orange and Ti^{4+} doped material is dark yellow.

The PXRD patterns comparing pure V$_2$O$_5$ to V$_{1.79}$Ba$_{0.21}$O$_5$ and V$_{1.81}$Ti$_{0.19}$O$_5$ obtained through electrospinning are shown in Figure 2(a) with appropriate reflection labelling for orthorhombic V$_2$O$_5$ [53], which is readily formed when subjected to a sufficient amount of oxidant or calcined in air to a high enough temperature [54]. Consequently, PXRD patterns results clearly show that orthorhombic

α-V_2O_5 is produced in an electrospinning process corresponding to the space group P*mmn* (ICSD 60767). The slight impurity detected in the PXRD for $V_{1.79}Ba_{0.21}O_5$, highlighted with an asterisk in Figure 2(a,b), is tentatively attributed to a phase separated compound of $Ba_3(VO_4)_2$ [55]. The PXRD pattern of $V_{1.81}Ti_{0.19}O_5$ sample shows no impure reflections indicating that a stable solid solution was formed [56].
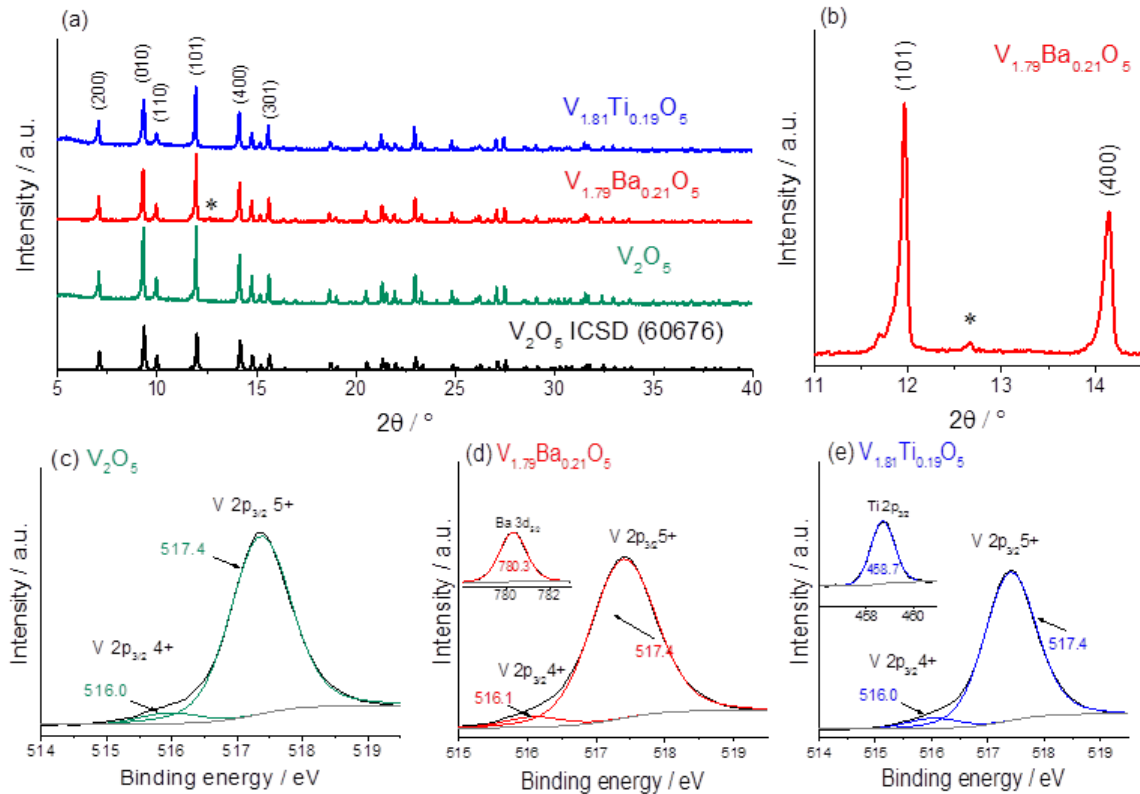

Figure 2: (a) PXRD patterns, Mo-source, for V_2O_5, $V_{1.79}Ba_{0.21}O_5$, and $V_{1.81}Ti_{0.19}O_5$ with a slight impurity highlighted with an asterisk at $2\theta = 12.7°$ for $V_{1.79}Ba_{0.21}O_5$. (b) enlarged region of impurity for $V_{1.79}Ba_{0.21}O_5$. XPS elemental scans of the (c) $V2p_{3/2}$ peak for V_2O_5. (d) $V2p_{3/2}$ peak and the $Ba3d_{5/2}$ peak for $V_{1.79}Ba_{0.21}O_5$ (inset). (e) $V2p_{3/2}$ peak and the $Ti2p_{3/2}$ peak for $V_{1.81}Ti_{0.19}O_5$ (inset).

Le Bail refinement results are shown in Table 1. Refinement of the PXRD patterns reveals an increase in the *a* and *b* directions for the doped samples compared to pure V_2O_5. The *c* direction increases for $V_{1.79}Ba_{0.21}O_5$ and decreases for $V_{1.81}Ti_{0.19}O_5$ when respectively compared to the pure V_2O_5. Overall $V_{1.81}Ti_{0.19}O_5$ has a smaller unit cell than the pure sample while the $V_{1.79}Ba_{0.21}O_5$ has a larger unit cell.

Table 1: Le Bail refinements of lattice parameters with the resultant unit cell volumes of V_2O_5, $V_{1.79}Ba_{0.21}O_5$, and $V_{1.81}Ti_{0.19}O_5$.

Sample	a (Å)	b (Å)	c (Å)	Volume (Å^3)	R_{wp} (%)
$V_{1.81}Ti_{0.19}O_5$	11.58(2)	3.57(7)	4.36(1)	180.86	10.17
$V_{1.79}Ba_{0.21}O_5$	11.58(3)	3.58(1)	4.41(1)	183.63	10.24
V_2O_5	11.54(1)	3.57(6)	4.39(2)	181.40	10.09

The same progression observed in the unit cell volumes is also seen in the d-spacings which were calculated using the [010] peak and Bragg's law with 4.08, 4.37, and 4.38 Å for $V_{1.81}Ti_{0.19}O_5$, V_2O_5, and $V_{1.79}Ba_{0.21}O_5$ respectively. A decrease in the interlayer spacing for $V_{1.81}Ti_{0.19}O_5$ can be attributed to a reduction in the electrostatic repulsion between the V_2O_5 layers caused by the Ti^{4+} shielding the negative charge associated with the apical oxygen atoms on the VO_5 pyramids [36,57,58]. This is a reasonable conclusion as the Ti^{4+} is larger (0.51 nm, CN = 5) than V^{5+} (0.46 nm, CN = 5) and hence could provide increased shielding. Ba^{2+} (1.35 nm, CN = 6) is significantly larger than V^{5+} which is reflected in an increased unit cell volume and likely distortion of the V_2O_5 layers.

XPS analysis of V_2O_5 in Figure 2(b) shows a $V^{4+}:V^{5+}$ ratio of 0.06:0.94. XPS analysis of $V_{1.79}Ba_{0.21}O_5$ in Figure 2(c,d) reveals a $V^{4+}:V^{5+}$ ratio of 0.05:0.95 and a $Ba^{2+}:V$ atomic ratio of 10.5:89.5 which is slightly higher than 8:92 as suggested by EDS. XPS analysis of $V_{1.81}Ti_{0.19}O_5$ in Figure 2(e.f) reveals a $V^{4+}:V^{5+}$ ratio of 0.06:0.94 and a $Ti^{4+}:V$ atomic ratio of 9.5:90.5 which is in good agreement with 10:90 as suggested by EDS. The variation in atomic ratios for $V_{1.79}Ba_{0.21}O_5$ is likely due to the precursor falling out of suspension during the electrospinning process as the Ba precursor, BaO, was less compatible with the ethanol solvent. Despite this, very little precursor was seen to fall out of the suspension, consequently the electrospinning process was allowed to continue. As the solubility limit of the sol-gel solution was surpassed, as evidenced by the suspension, it is likely that there is a higher concentration of Ba^{2+} at the surface of the microfibers.

The SEM images presented in Figure 3 reveal microscale fibers made up of nanoscale particles in a hierarchical structure. The fibers possess diameters of ≈1100 nm for V_2O_5 fibers (Figure 3(a,b)) a

range of 700-1000 nm for $V_{1.79}Ba_{0.21}O_5$ (Figure 3(c,d,e)) and $\approx$ 1660 nm for $V_{1.81}Ti_{0.19}O_5$ (Figure 3(f,g,h)). Interestingly, in Figure 3(e), there are some $V_{1.79}Ba_{0.21}O_5$ fibres that seem to be hollow. Conversely, the fibers are quite dense for $V_{1.81}Ti_{0.19}O_5$ and there appears to be a porous surface in the top right region of the SEM image in Figure 3(h). In some cases it appears that some of fibers have adhered together during the electrospinning operation. The larger diameters fibres in Figure 3(d) for $V_{1.79}Ba_{0.21}O_5$ and in Figure 3(g) for $V_{1.81}Ti_{0.19}O_5$ are approximately 1500 nm in size. This may be caused by inconsistencies in the electrospinning operation such as blockage of the needle, inhomogeneous sol gel, slow solvent evaporation or elevated humidity.
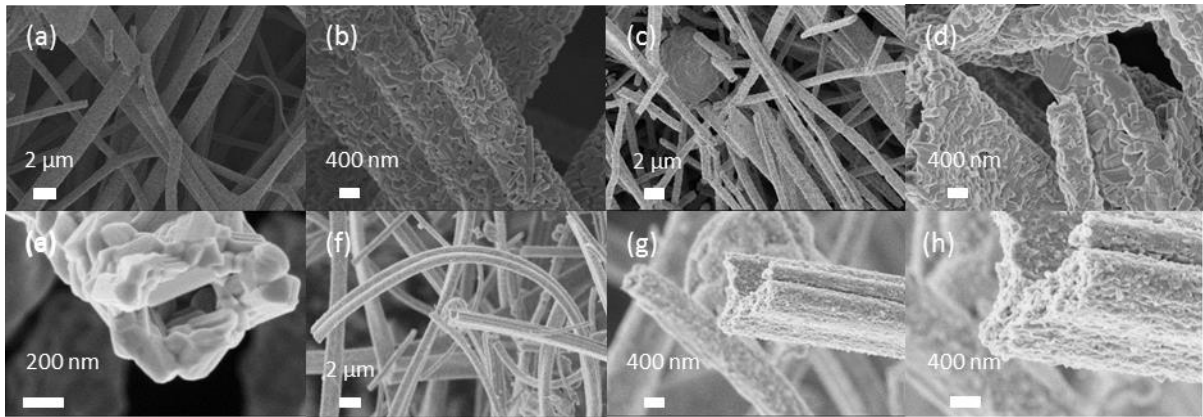

Figure 3: SEM images of (a-b) pure V_2O_5, (c-e) $V_{1.79}Ba_{0.21}O_5$., (f-h) $V_{1.81}Ti_{0.19}O_5$ highlighting the nanostructured microfibers produced via electrospinning.

Particle morphology of the microfibers was examined using TEM and was seen to substantially vary between materials, suggesting that particle morphology is heavily influenced by the addition of a dopant material as seen in Figure 4. The pure V_2O_5 fiber and particles (Figure 4(a,b,c)) are large and angular in appearance suggesting directional growth of the V_2O_5 layers with lengths of 240-260 nm and widths of 150-180 nm. The $V_{1.79}Ba_{0.21}O_5$ particles as seen in fiber TEM image in Figure 4(e) are needle-like in appearance and upon closer inspection possess widths of approximately 10 nm and lengths up to 1 µm (Figure 4(f,g)). The $V_{1.81}Ti_{0.19}O_5$ particles show a similar shape to those of pure V_2O_5 though smaller and less directional with dimensions ranging of 130-230 nm (Figure 4(j)). The porous particle surface suggested in Figure 3(h) is also observed in Figure 4(k) for $V_{1.81}Ti_{0.19}O_5$. In addition, lattice spacings are less defined in the $V_{1.79}Ba_{0.21}O_5$ material (Figure 4(h)) compared to V_2O_5

(Figure 4(d)) and $V_{1.81}Ti_{0.19}O_5$ (Figure 4(i)) with detected lattice spacings of 0.57 nm and 0.33 nm corresponding to the (200) and (101) plane for V_2O_5 and $V_{1.81}Ti_{0.19}O_5$, respectively.
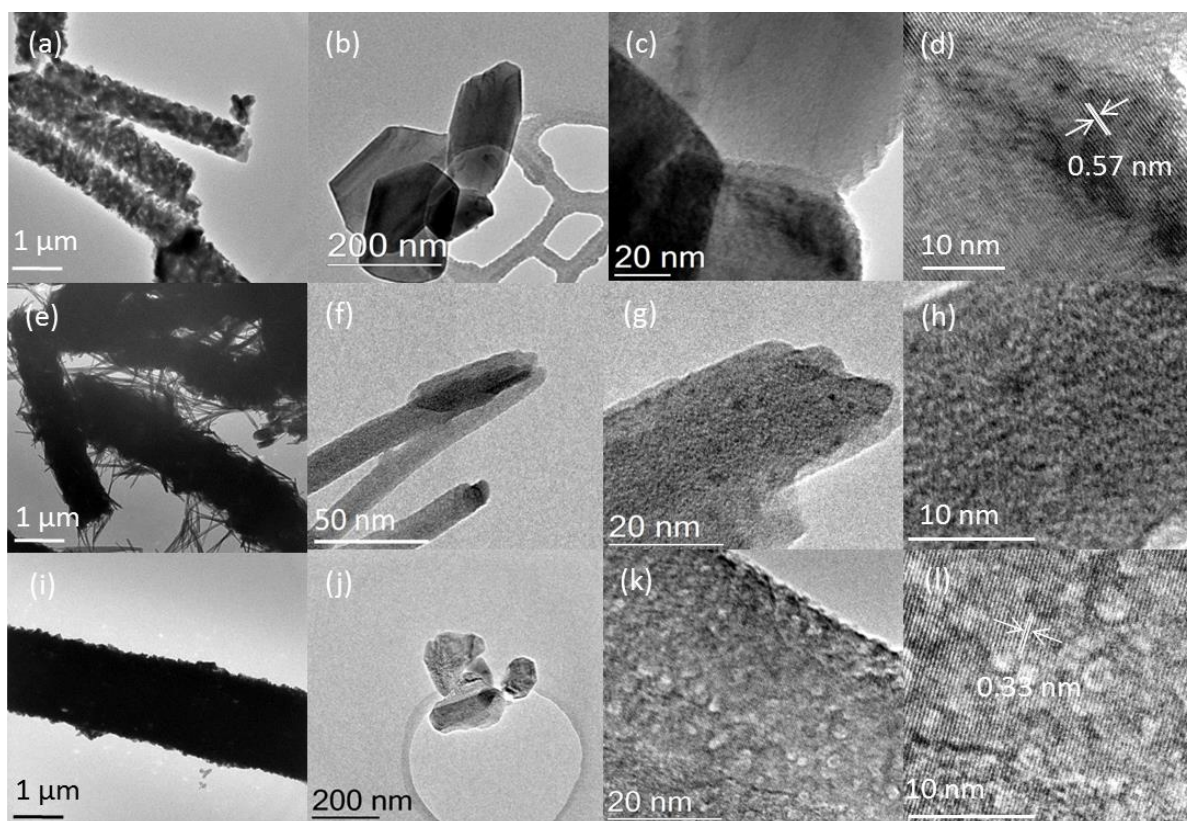

Figure 4: TEM images of (a) V_2O_5 microfibers, (b-c) V_2O_5 particles, (d) high resolution image of the V_2O_5 particle surface with lattice spacings highlighted, (e) $V_{1.79}Ba_{0.21}O_5$ microfibers, (f-g) $V_{1.79}Ba_{0.21}O_5$ particles, (h)) high resolution image of $V_{1.79}Ba_{0.21}O_5$ particle surface showing an absence of defined lattice spacings, (i) $V_{1.81}Ti_{0.19}O_5$ microfibers, (j-k) $V_{1.81}Ti_{0.19}O_5$ particles, (l) high resolution image of $V_{1.81}Ti_{0.19}O_5$ particle surface with lattice spacings highlighted.

BET specific surface area measurements for pure V_2O_5, $V_{1.79}Ba_{0.21}O_5$ and $V_{1.81}Ti_{0.19}O_5$ were 9.0, 12.8, and 19.3 m^2 g^{-1} respectively. While the variation between samples is not that great, it has been suggested that as crystallinity increases the surface area decreases [59]. This is reflected in the preceding structural analysis.

3.2 Electrochemical performance

Figure 5 details the cyclic voltammograms for the three materials and shows that the pure and doped materials possess oxidation and reduction peaks implying that the charge transfer mechanisms are predominantly redox-based with phase transitions that match α-V_2O_5, ε-$Li_{0.5}V_2O_5$, δ-LiV_2O_5, and γ-$Li_2V_2O_5$ using Figure 1(d).
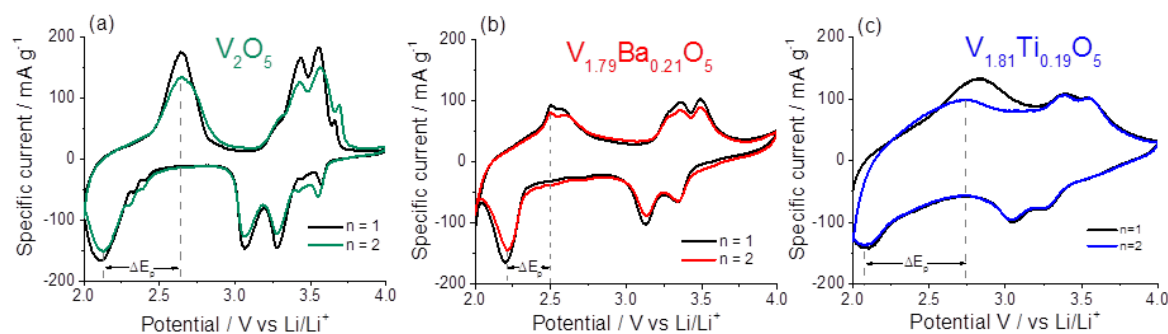
Figure 5: Cyclic voltammograms at 0.1 mV s^{-1} over 2 cycles with ΔE_p labelled for the δ/γ transition for (a) V_2O_5, (b) $V_{1.79}Ba_{0.21}O_5$ and (c) $V_{1.81}Ti_{0.19}O_5$.

Redox peak separations (ΔE_p) for the δ/γ transition, which are highlighted on the appropriate voltammogram, are 0.54, 0.30 and 0.65 V vs Li/Li$^+$ for V_2O_5, $V_{1.79}Ba_{0.21}O_5$, $V_{1.81}Ti_{0.19}O_5$, respectively. This suggests that the δ/γ transition is not favoured for $V_{1.81}Ti_{0.19}O_5$ due to the large ΔE_p implying that the Ti^{4+} dopant is hindering the phase transition. There is also a reduction in ΔE_p for the α/ε and ε/δ transitions in the doped materials compared to V_2O_5 indicating that Li-ion kinetics are improved for the doped materials along with reduced polarisation and higher reversibility [26]. The shoulder peaks on the pure V_2O_5 voltammogram at ca. 3.5 V vs Li/Li$^+$ indicate that the pure sample offers multiple Li-ion active sites for multi-stepped intercalation/extraction processes [60] and has a higher degree of crystallinity compared to the doped counterparts [18,19]. The absence of these shoulder peaks for both the $V_{1.79}Ba_{0.21}O_5$ and $V_{1.81}Ti_{0.19}O_5$ materials indicates that the complex structural changes occurring for V_2O_5 are reduced for the both doped counterparts [37]. Moreover, the $V_{1.81}Ti_{0.19}O_5$ voltammogram occupies a greater area than either V_2O_5 or $V_{1.79}Ba_{0.21}O_5$ which suggests that in

addition to diffusion controlled processes via Li-ion insertion there may be non-diffusion-controlled processes occurring resulting in increased storage capability [61].

Capacity vs potential plots for cycles 1, 5, 15 and 25 of the C-rate test are plotted for each sample in Figure 6. The initial discharge capacities seen in Figure 6(a) are 285 mAh g^{-1} ($\approx$1.9 mol of Li-ions) for V_2O_5, 136 mAh g^{-1} ($\approx$0.9 mol of Li-ions) for $V_{1.79}Ba_{0.21}O_5$, and 233 mAh g^{-1} ($\approx$1.6 mol of Li-ions) for $V_{1.81}Ti_{0.19}O_5$. These initial discharge capacities are reasonably comparable to theoretical capacity calculations (dopants amount determined via XPS analysis and the capacity was calculated based on the molar ratio of V in the overall sample) which are 294 mAh g^{-1} for pure V_2O_5, 239 mAh g^{-1} for $V_{1.79}Ba_{0.21}O_5$ and 267 mAh g^{-1} for $V_{1.81}Ti_{0.19}O_5$. The largest discrepancy is observed for $V_{1.79}Ba_{0.21}O_5$ which suggests that the Ba^{2+} is blocking active sites within the host V_2O_5 structure preventing effective Li-ion intercalation rendering a portion of the active material inactive.
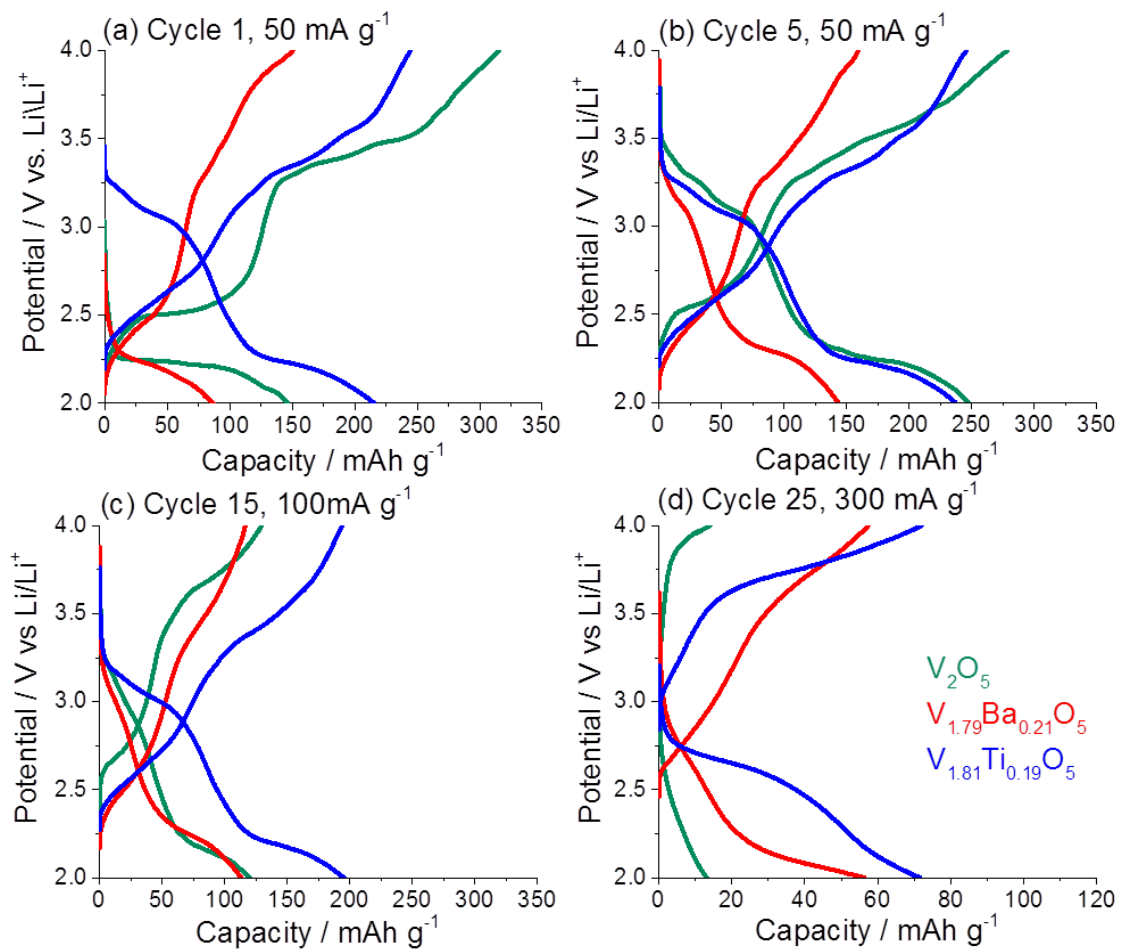
Figure 6: Capacity vs potential plots for all materials during the C-rate test for (a) the first cycle at 50 mA g^{-1}, (b) the fifth cycle at 50 mA g^{-1}, (c) the 15th cycle at 100 m Ag^{-1}, and (d) the 25th cycle at 300 mA g^{-1}.

Irreversible capacity loss (ICL) is variable for all materials with pure V_2O_5 experiencing the largest ICL of 169 mAh g^{-1} followed by $V_{1.79}Ba_{0.21}O_5$ at 64 mAh g^{-1} and $V_{1.81}Ti_{0.19}O_5$ with 29 mAh g^{-1}. The phase transitions in the V_2O_5 are quite distinct and can be assigned to α-V_2O_5, ε-$Li_{0.5}V_2O_5$, δ-LiV_2O_5, and γ-$Li_2V_2O_5$ referring to Figure 1(e). However, these phase transitions are less defined for the doped counterparts, though arguably still present. This is likely due to a dispersion of strain caused by the lithiation/delithiation process [62].

When the first charge capacity is higher than the first discharge it indicates that the excess capacity is due to interfacial storage across the electrolyte/electrode interface [39]. This implies that there is a large layer built up between the V_2O_5 and electrolyte which appears significantly reduced for both doped samples. A large ICL of 111 mAh g^{-1} was observed by Yu *et. al.* for pure V_2O_5 thin films compared to 36 mAh g^{-1} for Mn^{2+} doped V_2O_5 films [62]. The authors attributed this improvement in Li-ion intercalation/extraction of the Mn^{2+} doped film to the amorphisity of the films and increased oxygen vacancies providing nucleation centres for phase transitions.

The C-rate tests for the three materials are presented in Figure 7(a). Pure V_2O_5 undergoes high capacity losses over the initial 10 cycles at 50 mA g^{-1} with 285 mAh g^{-1} (n=2) which decreases to 185 mA g^{-1} (n=10) equating to a 35% loss. Conversely, $V_{1.79}Ba_{0.21}O_5$ and $V_{1.81}Ti_{0.19}O_5$ experienced no such capacity loss over the initial 10 cycles at 50 mA g^{-1}.
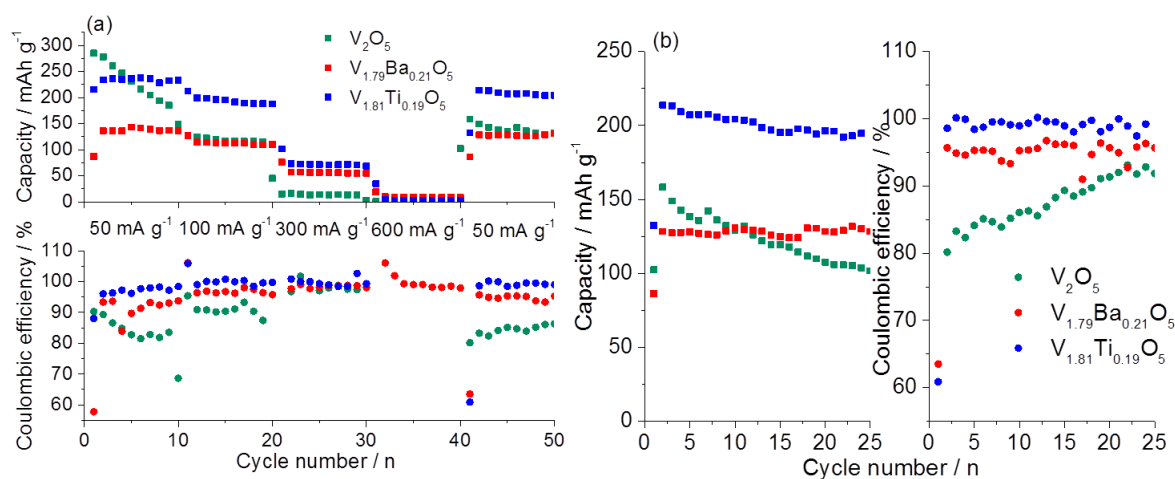
Figure 7: (a) C-rate test at various current rates with the relevant Coulombic efficiencies displayed below the C-rate test. (b) Cycling at 50 mA g^{-1} after the C-rate test detailed in 7(a) and relevant Coulombic efficiencies over 25 cycles displayed to the right of the cycling data.

Rate retention is variable between samples with a noticeable improvement between doped samples and pure V_2O_5 (Figure 7(a)). This variation in rate capability follows the same trend as the resultant surface areas with pure V_2O_5 showing the poorest rate performance and smallest surface area (9.0 m^{2}g^{-1}). Additionally, $V_{1.81}Ti_{0.19}O_5$ shows the best rate performance of the three samples with the highest surface area (19.3 m^{2}g^{-1}). V_2O_5 experiences a capacity loss of 50% from 230 mA g^{-1} (n=5, at 50 mA g^{-1}) to 117 mAh g^{-1} (n=15, at 100 mA g^{-1}) followed by a further 90% loss to 13 mAh g^{-1} (n=25, at 300 mA g^{-1}) between 100 mA g^{-1} and 300 mA g^{-1} current densities. After cycling at 600 mA g^{-1}, 85% of the original capacity is recovered at 158 mAh g^{-1} (n=42, at 50 mA g^{-1}) compared to 185 mAh g^{-1} (n=10, at 50 mA g^{-1}). There is an improvement in capacity retention for pure V_2O_5 between 50 mA g^{-1} and 100 mA g^{-1}. $V_{1.79}Ba_{0.21}O_5$ experiences a capacity loss of 20% from 140 mA g^{-1} (n=5, at 50 mA g^{-1}) to 112 mAh g^{-1} (n=15, at 100 mA g^{-1}) followed by a further 50% loss to 56 mAh g^{-1} (n=25, at 300 mA g^{-1}) between 100 mA g^{-1} and 300 mA g^{-1} current densities. After cycling at 600 mA g^{-1}, 94% of the original capacity is recovered at 128 mAhg^{-1} (n=42, at 50 mAg^{-1}) compared to 136 mAh g^{-1} (n=10, at 50 mA g^{-1}). $V_{1.81}Ti_{0.19}O_5$ experiences a capacity loss of 18% from 236 mAh g^{-1} (n=5, at 50 mA g^{-1}) to 195 mAh g^{-1} (n=15, at 100 mA g^{-1}) followed by a 64% loss to 71 mAh g^{-1} (n=25, at 300 mA g^{-1}) between 100 mA g^{-1} and 300 mA g^{-1} current densities. After cycling

18

at 600 mA g^{-1} 91% of the original capacity is recovered at 213 mAh g^{-1} (n=42, 50 mA g^{-1}) compared to 232 mAh g^{-1} (n=10, 50 mA g^{-1}).

After the C-rate tests, the samples were further cycled at a current density of 50 mA g^{-1}. Pure V$_2$O$_5$ retains 65% capacity from 158 mAh g^{-1} (n=2) to 102 mAh g^{-1} (n=25). V$_{1.79}$Ba$_{0.21}$O$_5$ experiences no overall capacity loss with 128 mAh g^{-1} obtained at n=2 and n=25. V$_{1.81}$Ti$_{0.19}$O$_5$ retains 91% capacity from 213 mAh g^{-1} (n=2) to 194 mAh g^{-1}. Average Coulombic efficiencies of samples over these cycles were 87% for V$_2$O$_5$, 95% for V$_{1.79}$Ba$_{0.21}$O$_5$ and 99% for V$_{1.81}$Ti$_{0.19}$O$_5$. Clearly V$_{1.79}$Ba$_{0.21}$O$_5$ and V$_{1.81}$Ti$_{0.19}$O$_5$ behaved much more efficiently than V$_2$O$_5$ as characterized by nearly 100% capacity retention compared to V$_2$O$_5$ in Figure 7(b).

The variation in obtained capacities is larger for the pure V$_2$O$_5$ and also has a higher initial capacity than that of the doped materials. This is expected as V$_2$O$_5$ is susceptible to substantial structural variations resulting in high capacity fading as more Li-ions can intercalate into the structure and cause more profound structural changes. This significant loss of capacity seen in the V$_2$O$_5$ material in the initial cycles has been confirmed by others [37,42]. Conversely, neither of the doped samples experience capacity losses over these initial 10 cycles indicating that the dopants provide a role in stabilizing the V$_2$O$_5$ structure. There is also an improvement in cycle stability for the doped materials compared to pure across all current rates. This is also observed to an extent in the voltammograms in Figure 5 as there is a greater overlap between cycles 1 and for V$_{1.79}$Ba$_{0.21}$O$_5$ and V$_{1.81}$Ti$_{0.19}$O$_5$ compared to pure V$_2$O$_5$.

All materials perform poorly at current rate of 600 mA g^{-1} which is reflected in virtually no capacity response at this current density clearly showing that these materials did not perform well under high rates. The poor capacity retention at 600 mA g^{-1} is likely due to a diffusion effect which implies that there is little to no interaction with the surface of the material at higher current densities. V$_2$O$_5$ has drawn wide attention as an electrode material, though its poor capacity retention and rate performance is caused by its low electronic conductivity and low Li-ion diffusion rate [63] which is clearly seen at

600 mA g^{-1}. Due to the poor capacity response at 600 mA g^{-1} for pure V_2O_5 and $V_{1.81}Ti_{0.19}O_5$ their Coulombic efficiencies have not been included in Figure 7(b).

Additionally, Coulombic efficiency was variable for all materials though noticeably improved for the doped materials in both the C-rate and cycling data implying that there is a prevention of Li-ion trapping in the $V_{1.79}Ba_{0.21}O_5$ and $V_{1.81}Ti_{0.19}O_5$ materials. Despite this, the Coulombic efficiencies are still quite variable at lower rates, such as 50 mA g^{-1}, which is likely caused by increased side reactions.

In order to closely examine what occurred during the first cycling process ex-situ XRDs were obtained after the first lithiation to 2.0 V vs Li/Li$^+$ and the first delithiation to 4.0 V vs Li/Li$^+$ for V_2O_5 and $V_{1.81}Ti_{0.19}O_5$ as shown in Figure 8(a) and 8(b) respectively. The coin cells were dismantled in an argon-filled glovebox and the electrodes were rinsed with DMC before ex-situ XRD was undertaken. $V_{1.79}Ba_{0.21}O_5$ has not been examined as this dopant did not drastically improve the electrochemical performance of V_2O_5 as evidence by both the C-rate and cycling data.
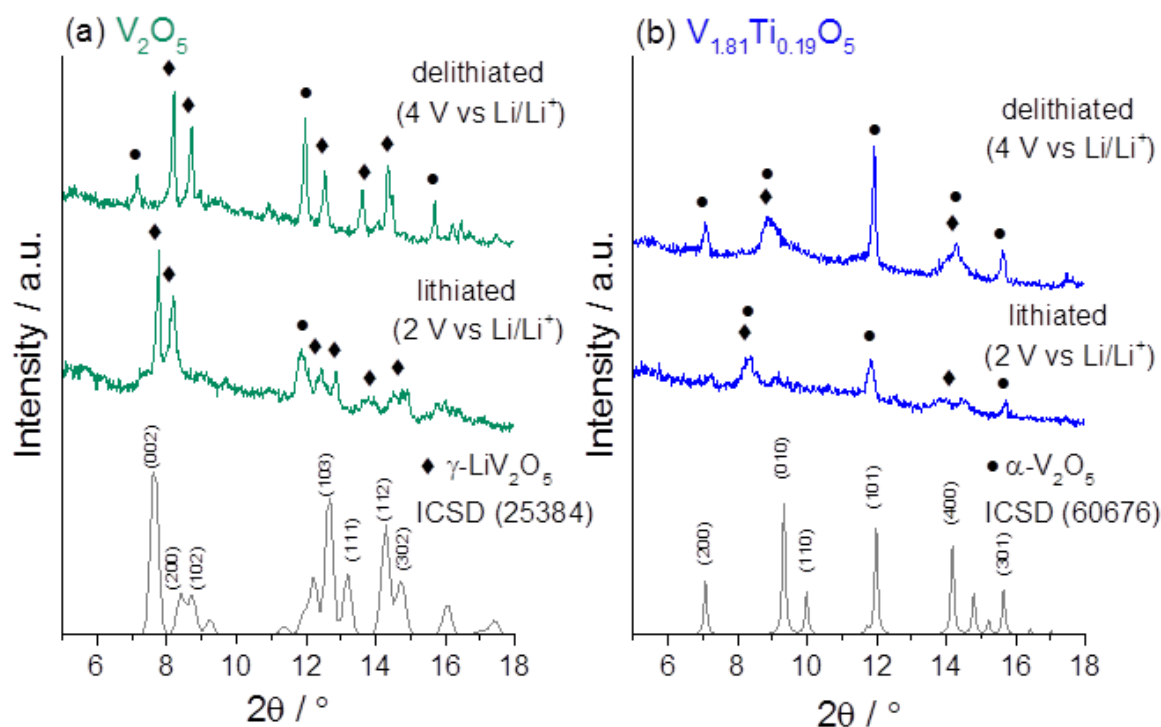
Figure 8: Ex-situ XRD of the lithiated (2 V *vs* Li/Li$^+$) and delithiated (4 V *vs* Li/Li$^+$) states (a) showing a higher proportion of γ-LiV$_2$O$_5$ (♦) for V$_2$O$_5$ and (b) a higher proportion of α-V$_2$O$_5$ (●) for V$_{1.81}$Ti$_{0.19}$O$_5$.

Both V$_2$O$_5$ and V$_{1.81}$Ti$_{0.19}$O$_5$ have lower reflection intensities at both 2.0 V vs Li/Li$^+$ and 4.0V vs Li/Li$^+$ compared to the pristine powder, as seen in Figure 2(b), which is indicative of a decrease in crystallite size [64,65]. Reflection shift variation between the lithiated and delithiated states is largest for V$_2$O$_5$ indicating a significant shift in the V$_2$O$_5$ layers as seen in an interlayer distance reduction after extraction of Li-ions from the material. V$_{1.81}$Ti$_{0.19}$O$_5$ has smaller reflection variations implying that this material experiences increased structural stabilization [52] which has been observed in both the C-rate and cycling results, detailed in Figure 7(a) and 7(b).

The (200) peak at 2θ = 7° disappears at the lithiated (2.0 V vs Li/Li$^+$) stage and then returns at the delithiated (4.0 V vs Li/Li$^+$) stage for both materials which is an indication of disordering of the V$_2$O$_5$ structure during lithiation and reordering during delithiation caused by the intercalation/extraction of Li-ions.

The PXRDs for the lithiated (2.0 V vs Li/Li$^+$) and delithiated (4.0 V vs Li/Li$^+$) states of V$_2$O$_5$ clearly show a mix of both α-V$_2$O$_5$, the orthorhombic unintercalated phase, and γ-LiV$_2$O$_5$ with a space group of *Pnma* [66] that has been known to irreversibly form in the 2-2.7 V vs Li/Li$^+$ range resulting in capacity fading. Conversely, the reflections of V$_{1.81}$Ti$_{0.19}$O$_5$ at the lithiated (2.0 V vs Li/Li$^+$) and delithiated (4.0 V *vs* Li/Li$^+$) states can be attributed to a higher proportion of orthorhombic V$_2$O$_5$ than that of the γ-LiV$_2$O$_5$ indicating that the Ti^{4+} dopant provides increased stabilization and promotes higher degree of reversibility in the facilitation of phase changes. The absence of ε-Li$_{0.5}$V$_2$O$_5$ and δ-LiV$_2$O$_5$ suggests that these intermediate phases were reversibly formed and that a complete conversion of them occurred during the first lithiation at 2.0 V vs Li/Li$^+$ and the first delithiation at 4.0 V vs Li/Li$^+$.

The large ΔE$_P$ value for the δ/γ transition for V$_{1.81}$Ti$_{0.19}$O$_5$ (Figure 5(c)) not only suggests that this transition is not favoured but is also in agreement with the ex-situ XRD (Figure 8(b)) that possess a

smaller proportion of γ- LiV_2O_5 compared to α-V_2O_5. Moreover, the large irreversible capacity loss seen for pureV_2O_5 in the capacity vs potential plots (Figure 6) is most likely a result of the high proportion of γ-LiV_2O_5 formed in this material and large structural variations resulting from the build-up of Li-ions at the electrode/electrolyte interface.

The results presented herein indicate that the improved electrochemical performance of the titanium-doped sample can be found in the suppressed irreversible phase transformation towards γ-LiV_2O_5 as shown by Ex-situ PXRDs and CV cycling data. This shows that focussing on the improvement of material performance via use of dopants for structural stabilization is a worthwhile path of investigation.

4. Conclusion

Electrospinning is a versatile and effective method for producing one-dimensional fibers consisting of nanostructured particles from sol gel solutions. V_2O_5, $V_{1.79}Ba_{0.21}O_5$ and $V_{1.81}Ti_{0.19}O_5$ were produced in a simple electrospinning process followed by a single pyrolysis step and were investigated as positive electrodes for Li ion coin cells (*vs* Li metal). Both dopant materials offered increased stabilization of the V_2O_5 and rendered the V_2O_5 structure less susceptible to distortion caused by the intercalation/extraction of the Li-ions. This was observed in an improvement in cycle stabilities and Coulombic efficiencies. Ti^{4+} was shown to be a suitable redox-inactive dopant providing increased structural stabilization with cycling via phase change prevention.

References

[1] S. Holmberg, A. Perebikovsky, L. Kulinsky, M. Madou, 3-D Micro and Nano Technologies for Improvements in Electrochemical Power Devices, Micromachines. 5 (2014) 171–203.

[2] S. Wilke, B. Schweitzer, S. Khateeb, S. Al-Hallaj, Preventing thermal runaway propagation in lithium ion battery packs using a phase change composite material: An experimental study, J. Power Sources. 340 (2017) 51–59.

[3] W. Lv, Y. Niu, X. Jian, K.H.L. Zhang, W. Wang, J. Zhao, Z. Wang, W. Yang, W. He, Space matters: Li^+ conduction versus strain effect at $FePO_4$ /$LiFePO_4$ interface, Appl. Phys. Lett. 108 (2016) 83901.

[4] G. Zhu, K. Wen, W. Lv, X. Zhou, Y. Liang, F. Yang, Z. Chen, M. Zou, J. Li, Y. Zhang, W. He, Materials insights into low-temperature performances of lithium-ion batteries, J. Power Sources. 300 (2015) 29–40.

[5] S.-W. Baek, I. Honma, J. Kim, D. Rangappa, Solidified inorganic-organic hybrid electrolyte for all solid state flexible lithium battery, J. Power Sources. 343 (2017) 22–29.

[6] M.V. Reddy, G.V. Subba Rao, B.V.R. Chowdari, Metal Oxides and Oxysalts as Anode Materials for Li Ion Batteries, Am. Chem. Soc. 113 (2013) 5364–5457.

[7] M.V. Reddy, G.V. Subba Rao, B.V.R. Chowdari, Long-term cycling studies on 4 V-cathode, lithium vanadium fluorophosphate, J. Power Sources. 195 (2010) 5768–5774.

[8] D. Liu, J. Han, J.B. Goodenough, Structure, morphology, and cathode performance of Li1−x[Ni0.5Mn1.5]O4 prepared by coprecipitation with oxalic acid, J. Power Sources. 195 (2010) 2918–2923.

[9] S. Kraas, A. Vijn, M. Falk, B. Ufer, B. Luerßen, J. Janek, M. Fröba, Nanostructured and nanoporous LiFePO4 and LiNi0.5Mn1.5O4-δ as cathode materials for lithium-ion batteries, Funct. Mater. Anal. High Perform. Lithium Ion Batter. 42 (2014) 218–241.

[10] B. Pei, Z. Jiang, W. Zhang, Z. Yang, A. Manthiram, Nanostructured Li3V2(PO4)3 cathode supported on reduced graphene oxide for lithium-ion batteries, J. Power Sources. 239 (2013) 475–482.

[11] A.S. Arico, P. Bruce, B. Scrosati, J.-M. Tarascon, W. van Schalkwijk, Nanostructured materials for advanced energy conversion and storage devices, Nat Mater. 4 (2005) 366–377.

[12] L. Mai, L. Xu, C. Han, X. Xu, Y. Luo, S. Zhao, Y. Zhao, Electrospun Ultralong Hierarchical Vanadium Oxide Nanowires with High Performance for Lithium Ion Batteries, Nano Lett. 10 (2010) 4750–4755.

[13] H.-E. Wang, D.-S. Chen, Y. Cai, R.-L. Zhang, J.-M. Xu, Z. Deng, X.-F. Zheng, Y. Li, I. Bello, B.-L. Su, Facile synthesis of hierarchical and porous V2O5 microspheres as cathode materials for lithium ion batteries, J. Colloid Interface Sci. 418 (2014) 74–80.

[14] Liqiang Mai, Qiulong Wei, Xiaocong Tian, Yunlong Zhao, Qinyou An, Electrochemical Nanowire Devices for Energy Storage, IEEE Trans. Nanotechnol. 13 (2014) 10–15.

[15] D. McNulty, D.N. Buckley, C. O'Dwyer, Synthesis and electrochemical properties of vanadium oxide materials and structures as Li-ion battery positive electrodes, J. Power Sources. 267 (2014) 831–873.

[16] T. Zhai, H. Liu, H. Li, X. Fang, M. Liao, L. Li, H. Zhou, Y. Koide, Y. Bando, D. Golberg, Centimeter-Long V2O5 Nanowires: From Synthesis to Field-Emission, Electrochemical, Electrical Transport, and Photoconductive Properties, Adv. Mater. 22 (2010) 2547–2552.

[17] S.Y. Zhan, C.Z. Wang, K. Nikolowski, H. Ehrenberg, G. Chen, Y.J. Wei, Electrochemical properties of Cr doped V2O5 between 3.8 V and 2.0 V, Solid State Ion. 180 (2009) 1198–1203.

[18] A. Pan, J.-G. Zhang, Z. Nie, G. Cao, B.W. Arey, G. Li, S. Liang, J. Liu, Facile synthesized nanorod structured vanadium pentoxide for high-rate lithium batteries, J. Mater. Chem. 20 (2010) 9193.

[19] H. Zhao, L. Pan, S. Xing, J. Luo, J. Xu, Vanadium oxides–reduced graphene oxide composite for lithium-ion batteries and supercapacitors with improved electrochemical performance, J. Power Sources. 222 (2013) 21–31.

[20] C. Delmas, H. Cognac-Auradou, J.M. Cocciantelli, M. Ménétrier, J.P. Doumerc, The LixV2O5 system: An overview of the structure modifications induced by the lithium intercalation, Solid State Ion. 69 (1994) 257–264.

[21] Yan L. Cheah, V. Aravindan, Srinivasan Madhavi, Chemical Lithiation Studies on Combustion Synthesized V2O5 Cathodes with Full Cell Application for Lithium Ion Batteries, J. Electrochem. Soc. 160 (2013) A1016–A1024.

[22] X. Li, W. Li, H. Ma, J. Chen, Electrochemical Lithium Intercalation/Deintercalation of Single-Crystalline V2O5 Nanowires, J. Electrochem. Soc. 154 (2007) A39–A42.

[23] M. Winter, J.O. Besenhard, M.E. Spahr, P. Novak, Insertion Electrode Materials for Rechargeable Lithium Batteries, Adv. Mater. 10 (1998).

[24] K. Zhu, Y. Meng, H. Qiu, Y. Gao, C. Wang, F. Du, Y. Wei, G. Chen, C. Wang, G. Chen, Facile synthesis of V2O5 nanoparticles as a capable cathode for high energy lithium-ion batteries, J. Alloys Compd. 650 (2015) 370–373.

[25] S. Liang, M. Qin, Y. Tang, Q. Zhang, X. Li, X. Tan, A. Pan, Facile synthesis of nanosheet-structured V2O5 with enhanced electrochemical performance for high energy lithium-ion batteries, Met. Mater. Int. 20 (2014) 983–988.

[26] M. Qin, J. Liu, S. Liang, Q. Zhang, X. Li, Y. Liu, M. Lin, Facile synthesis of multiwalled carbon nanotube–V2O5 nanocomposites as cathode materials for Li-ion batteries, J. Solid State Electrochem. 18 (2014) 2841–2846.

[27] I.D. Johnson, E. Blagovidova, P.A. Dingwall, D.J.L. Brett, P.R. Shearing, J.A. Darr, High power Nb-doped LiFePO4 Li-ion battery cathodes; pilot-scale synthesis and electrochemical properties, J. Power Sources. 326 (2016) 476–481.

[28] S.-Y. Chung, J.T. Bloking, Y.-M. Chiang, Electronically conductive phospho-olivines as lithium storage electrodes, Nat Mater. 1 (2002) 123–128.

[29] K. Hoang, M.D. Johannes, First-principles studies of the effects of impurities on the ionic and electronic conduction in LiFePO4, J. Power Sources. 206 (2012) 274–281.

[30] C.H. Chen, J. Liu, M.E. Stoll, G. Henriksen, D.R. Vissers, K. Amine, Aluminum-doped lithium nickel cobalt oxide electrodes for high-power lithium-ion batteries, J. Power Sources. 128 (2004) 278–285.

[31] P. Kalyani, N. Kalaiselvi, Various aspects of LiNiO2 chemistry: A review, Sci. Technol. Adv. Mater. 6 (2005) 689–703.

[32] H. Arai, S. Okada, Y. Sakurai, J. Yamaki, Thermal behavior of Li1−yNiO2 and the decomposition mechanism, Solid State Ion. 109 (1998) 295–302.

[33] N. Nitta, F. Wu, J.T. Lee, G. Yushin, Li-ion battery materials: present and future, Mater. Today. 18 (2015) 252–264.

[34] S. Zhan, G. Chen, D. Liu, A. Li, C. Wang, Y. Wei, Effects of Cr doping on the structural and electrochemical properties of V2O5, J. Alloys Compd. 479 (2009) 652–656.

[35] Y. Wu, P. Zhu, X. Zhao, M.V. Reddy, S. Peng, B.V.R. Chowdari, S. Ramakrishna, Highly improved rechargeable stability for lithium/silver vanadium oxide battery induced viaelectrospinning technique, J Mater Chem A. 1 (2013) 852–859.

[36] F. Coustier, J. Hill, B.B. Owens, S. Passerini, W.H. Smyrl, Doped vanadium oxides as host materials for lithium intercalation, J. Electrochem. Soc. 146 (1999) 1355–1360.

[37] Y. Wei, C.-W. Ryu, K.-B. Kim, Improvement in electrochemical performance of V2O5 by Cu doping, J. Power Sources. 165 (2007) 386–392.

[38] S. Zhan, Y. Wei, X. Bie, C. Wang, F. Du, G. Chen, F. Hu, Structural and electrochemical properties of Al3+ doped V2O5 nanoparticles prepared by an oxalic acid assisted soft-chemical method, J. Alloys Compd. 502 (2010) 92–96.

[39] Y.L. Cheah, V. Aravindan, S. Madhavi, Improved Elevated Temperature Performance of Al-Intercalated V2O5 Electrospun Nanofibers for Lithium-Ion Batteries, ACS Appl. Mater. Interfaces. 4 (2012) 3270–3277.

[40] A. Sakunthala, M.V. Reddy, S. Selvasekarapandian, B.V.R. Chowdari, P.C. Selvin, Energy storage studies of bare and doped vanadium pentoxide, (V1.95M0.05)O5, M = Nb, Ta, for lithium ion batteries, Energy Environ. Sci. 4 (2011) 1712–1725.

[41] S. Liang, J. Zhou, G. Fang, C. Zhang, J. Wu, Y. Tang, A. Pan, Synthesis of mesoporous β-Na0.33V2O5 with enhanced electrochemical performance for lithium ion batteries, Electrochimica Acta. 130 (2014) 119–126.

[42] S.-R. Li, S.-Y. Ge, Y. Qiao, Y.-M. Chen, X.-Y. Feng, J.-F. Zhu, C.-H. Chen, Three-dimensional porous Fe0.1V2O5.15 thin film as a cathode material for lithium ion batteries, Electrochimica Acta. 64 (2012) 81–86.

[43] P.H. Jampani, O. Velikokhatnyi, K. Kadakia, D.H. Hong, S.S. Damle, J.A. Poston, A. Manivannan, P.N. Kumta, High energy density titanium doped-vanadium oxide-vertically aligned CNT composite electrodes for supercapacitor applications, J Mater Chem A. 3 (2015) 8413–8432.

[44] K. Takahashi, Y. Wang, K. Lee, G. Cao, Fabrication and Li+-intercalation properties of V2O5-TiO2 composite nanorod arrays, Appl. Phys. A. 82 (2006) 27–31.

[45] P. Nithyadharseni, M.V. Reddy, K.I. Ozoemena, F.I. Ezema, R.G. Balakrishna, B.V.R. Chowdari, Electrochemical Performance of BaSnO3 Anode Material for Lithium-Ion Battery Prepared by Molten Salt Method, J. Electrochem. Soc. 163 (2016) A540–A545.

[46] N. Sharma, K.M. Shaju, G.V.S. Rao, B.V.R. Chowdari, Anodic behaviour and X-ray photoelectron spectroscopy of ternary tin oxides, J. Power Sources. 139 (2005) 250–260.

[47] V. Modafferi, S. Trocino, A. Donato, G. Panzera, G. Neri, Electrospun V2O5 composite fibers: Synthesis, characterization and ammonia sensing properties, Thin Solid Films. 548 (2013) 689–694.

[48] P. Zhu, Y. Wu, M.V. Reddy, A. Sreekumaran Nair, B.V.R. Chowdari, S. Ramakrishna, Long term cycling studies of electrospun TiO2 nanostructures and their composites with MWCNTs for rechargeable Li-ion batteries, RSC Adv. 2 (2012) 531–537.

[49] S. Beke, A review of the growth of V2O5 films from 1885 to 2010, Thin Solid Films. 519 (2011) 1761–1771.

[50] Y.L. Cheah, N. Gupta, S.S. Pramana, V. Aravindan, G. Wee, M. Srinivasan, Morphology, structure and electrochemical properties of single phase electrospun vanadium pentoxide nanofibers for lithium ion batteries, J. Power Sources. 196 (2011) 6465–6472.

[51] L. Liang, M. Zhou, Y. Xie, Electrospun Hierarchical LiV3O8 Nanofibers Assembled from Nanosheets with Exposed 100 Facets and their Enhanced Performance in Aqueous Lithium-Ion Batteries, Chem. – Asian J. 7 (2012) 565–571.

[52] J.J. Yu, J. Yang, W.B. Nie, Z.H. Li, E.H. Liu, G.T. Lei, Q.Z. Xiao, A porous vanadium pentoxide nanomaterial as cathode material for rechargeable lithium batteries, Electrochimica Acta. 89 (2013) 292–299.

[53] V. Shklover, T. Haibach, R. Nespar, P. Novak, F. Reid, Crystal structure of the produce of Mg2+ insertion into V2O5 single crystals Locality: synthetic Sample:IIb, J. Solid State Chem. 123 (1996) 317–323.

[54] C. Wu, H. Wei, B. Ning, Y. Xie, New Vanadium Oxide Nanostructures: Controlled Synthesis and Their Smart Electrical Switching Properties, Adv. Mater. 22 (2010) 1972–1976.

[55] The structure of Ba3(VO4)2, Z. Für Krist. 131 (2010) 161.

[56] J. Liu, W. Guo, F. Qu, C. Feng, C. Li, L. Zhu, J. Zhou, S. Ruan, W. Chen, V-doped In2O3 nanofibers for H2S detection at low temperature, Ceram. Int. 40 (2014) 6685–6689.

[57] H.X. Li, L.F. Jiao, H.T. Yuan, M. Zhao, M. Zhang, Y.M. Wang, High-performance Cu-doped vanadium oxide (CuxV2O5) prepared by rapid precipitation method for rechargeable batteries, Mater. Lett. 61 (2007) 101–104.

[58] D. Zhu, H. Liu, L. Lv, Y.D. Yao, W.Z. Yang, Hollow microspheres of V2O5 and Cu-doped V2O5 as cathode materials for lithium-ion batteries, Scr. Mater. 59 (2008) 642–645.

[59] S.-Z. Huang, Y. Cai, J. Jin, Y. Li, X.-F. Zheng, H.-E. Wang, M. Wu, L.-H. Chen, B.-L. Su, Annealed vanadium oxide nanowires and nanotubes as high performance cathode materials for lithium ion batteries, J. Mater. Chem. A. 2 (2014) 14099.

[60] J. Kawakita, M. Majima, T. Miura, T. Kishi, Preparation and lithium insertion behaviour of oxygen-deficient $Li_{1+x}V_3O_{8-\delta}$, J. Power Sources. 66 (1997) 135–139.

[61] M. Sathiya, A.S. Prakash, K. Ramesha, J. Tarascon, A.K. Shukla, V2O5-Anchored Carbon Nanotubes for Enhanced Electrochemical Energy Storage, J. Am. Chem. Soc. 133 (2011) 16291–16299.

[62] D.M. Yu, S.T. Zhang, D.W. Liu, X.Y. Zhou, S.H. Xie, Q.F. Zhang, Y.Y. Liu, G.Z. Cao, Effect of manganese doping on Li-ion intercalation properties of V2O5 films, J. Mater. Chem. 20 (2010) 10841.

[63] S.H. Choi, Y.C. Kang, Uniform Decoration of Vanadium Oxide Nanocrystals on Reduced Graphene-Oxide Balls by an Aerosol Process for Lithium-Ion Battery Cathode Material, Chem. - Eur. J. 20 (2014) 6294–6299.

[64] W.J.H. Borghols, M. Wagemaker, U. Lafont, E.M. Kelder, F.M. Mulder, Impact of Nanosizing on Lithiated Rutile TiO2, Chem. Mater. 20 (2008) 2949–2955.

[65] Y.-S. Hu, L. Kienle, Y.-G. Guo, J. Maier, High Lithium Electroactivity of Nanometer-Sized Rutile TiO2, Adv. Mater. 18 (2006) 1421–1426.

[66] J. Galy, Vanadium pentoxide and vanadium oxide bronzes—Structural chemistry of single (S) and double (D) layer MxV2O5 phases, J. Solid State Chem. 100 (1992) 229–245.